Applied Physics Letters

RESEARCH ARTICLE | JULY 24 2023

Temperature-dependent thermal conductivity of MBE-grown epitaxial $SrSnO_3$ films

Chi Zhang ; Fengdeng Liu ; Silu Guo ; Yingying Zhang ; Xiaotian Xu ; K. Andre Mkhoyan ; Bharat Jalan ; Xiaojia Wang

Check for updates

Appl. Phys. Lett. 123, 042201 (2023)
https://doi.org/10.1063/5.0156367

View Online
Export Citation

13 May 2024 18:59:04

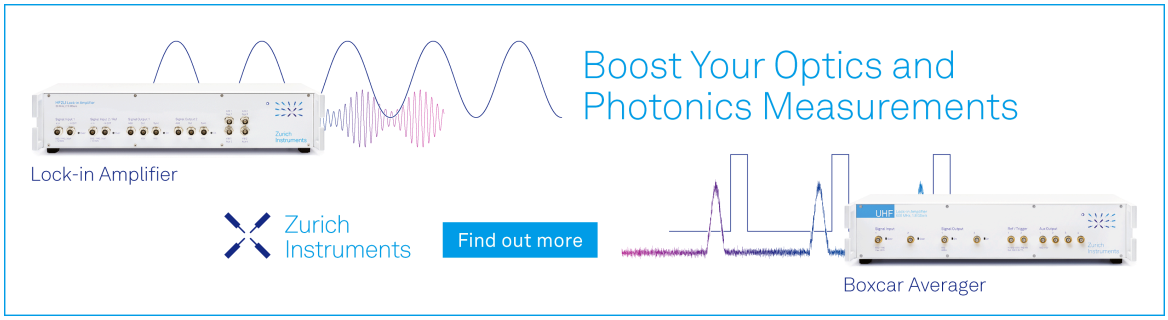

AIP Publishing

Applied Physics Letters ARTICLE pubs.aip.org/aip/apl

Temperature-dependent thermal conductivity of MBE-grown epitaxial $SrSnO_3$ films

Cite as: Appl. Phys. Lett. **123**, 042201 (2023); doi: 10.1063/5.0156367
Submitted: 28 April 2023 · Accepted: 7 July 2023 ·
Published Online: 24 July 2023

View Online Export Citation CrossMark

Chi Zhang,[1] Fengdeng Liu,[2,3] Silu Guo,[2] Yingying Zhang,[1] Xiaotian Xu,[1] K. Andre Mkhoyan,[2] Bharat Jalan,[2] and Xiaojia Wang[1,a)]

AFFILIATIONS

[1]Department of Mechanical Engineering, University of Minnesota, Minneapolis, Minnesota 55455, USA
[2]Department of Chemical Engineering and Materials Science, University of Minnesota, Minneapolis, Minnesota 55455, USA
[3]Department of Electrical and Computer Engineering, University of Minnesota, Minneapolis, Minnesota 55455, USA

[a)]Author to whom correspondence should be addressed: wang4940@umn.edu

ABSTRACT

As an ultrawide bandgap (~4.1 eV) semiconductor, single crystalline $SrSnO_3$ (SSO) has promising electrical properties for applications in power electronics and transparent conductors. The device performance can be limited by heat dissipation issues. However, a systematic study detailing its thermal transport properties remains elusive. This work studies the temperature-dependent thermal properties of a single crystalline SSO thin film prepared with hybrid molecular beam epitaxy. By combining time-domain thermoreflectance and Debye–Callaway modeling, physical insight into thermal transport mechanisms is provided. At room temperature, the 350-nm SSO film has a thermal conductivity of 4.4 W m^{-1} K^{-1}, ~60% lower than those of other perovskite oxides ($SrTiO_3$, $BaSnO_3$) with the same ABO_3 structural formula. This difference is attributed to the low zone-boundary frequency of SSO, resulting from its distorted orthorhombic structure with tilted octahedra. At high temperatures, the thermal conductivity of SSO decreases with temperature following a $\sim T^{-0.54}$ dependence, weaker than the typical T^{-1} trend dominated by the Umklapp scattering. This work not only reveals the fundamental mechanisms of thermal transport in single crystalline SSO but also sheds light on the thermal design and optimization of SSO-based electronic applications.

Published under an exclusive license by AIP Publishing. https://doi.org/10.1063/5.0156367

Owing to wide bandgaps and excellent dopability with reasonably high room-temperature (RT) electron mobilities, perovskite alkaline-earth stannates have recently fascinated researchers for potential applications in power electronics and transparent displays. Particularly, bulk barium stannate ($BaSnO_3$, BSO), with a bandgap of ~3 eV, has been reported to have an RT mobility of 320 cm^2 V^{-1} s^{-1}.[1] However, the highest RT electron mobility of BSO thin films is limited to 183 cm^2 V^{-1} s^{-1} according to the literature.[2] The lower RT electron mobility of BSO thin films is attributed to its high threading dislocation density resulting from the large film/substrate lattice mismatch.[2–4] Unlike BSO, the smaller lattice parameters of strontium stannate ($SrSnO_3$, SSO) allow a better lattice match between the film and substrate, enabling coherent growth on commercially available substrates.[5,6] The highest reported RT mobility in doped SSO films is 70 cm^2 V^{-1} s^{-1} at a carrier density of 2×10^{20} cm^{-3}, lower than that of BSO.[2] However, SSO adds the benefit of offering a wider bandgap (~4.1 eV), reaching the ultrawide bandgap (UWBG) regime.[7–9] It is also worth noting that doped SSO possesses the higher RT mobility at high carrier densities ($>10^{19}$ cm^{-3}) among all known UWBG semiconductors.[10] For these reasons, SSO films hold great potential as a UWBG semiconductor for power electronics.[11]

For typical semiconductor-based electronic applications, heat dissipation is critical, and thus, the thermal properties of semiconductors, as building blocks for devices, need to be carefully examined. Unlike other perovskite oxides, such as BSO,[12,13] strontium titanate ($SrTiO_3$, STO),[14,15] and lanthanum aluminate ($LaAlO_3$, LAO),[16,17] literature studies of the thermal properties of SSO remain elusive, despite its intriguing electronic properties and great potential in electronic applications. To date, only one group reported the thermal conductivity of ~4.5 W m^{-1} K^{-1} for polycrystalline SSO with the grain sizes of several micrometers to 10 μm.[18] The limitation of reporting SSO thermal properties is partially attributed to the challenge in synthesizing high-quality single crystalline SSO films with controlled structure and doping. Only recently, it has been demonstrated that hybrid molecular beam epitaxy (MBE) can produce single crystalline SSO with controlled doping and improved structural quality.[6,19] This allows for the exploration of the thermal properties of UWBG single crystalline SSO. Building upon the synthesis advancements, we perform a systematic

13 May 2024 18:59:04

Published under an exclusive license by AIP Publishing

study of the thermal properties of the single crystalline SSO film prepared with hybrid MBE by integrating time-domain thermoreflectance (TDTR) measurements and theoretical model analyses. The comparison of measurement data with the Debye–Callaway model calculations enables the establishment of a structure-thermal property relationship for this class of perovskites.

Single crystalline SSO films were grown on a STO (001) substrate (CrysTec) with the hybrid MBE approach (Sec. 1 of the supplementary material). After growth, high-resolution x-ray diffraction (HRXRD) 2θ-ω coupled scans (Rigaku SmartLab XE) were used for structural characterization and the determination of out-of-plane lattice parameters. The schematics of SSO and STO lattice structures are shown in Fig. 1(a), highlighting an orthorhombically distorted feature of SSO compared to the cubic STO. Figure 1(b) shows an on-axis HRXRD 2θ-ω couple scan of the SSO film on the STO (001) substrate, indicating the phase-pure single crystalline SSO film. The out-of-plane lattice parameter is 4.038 Å, comparable to a bulk value of ~4.035 Å, suggesting a fully relaxed orthorhombic phase for the SSO film.[20,21] To evaluate the thickness and crystalline structure of the SSO film, cross-sectional samples for scanning transmission electron microscopy (STEM) characterization were prepared with a focused ion beam (Sec. 2 of the supplementary material). A high-angle annular dark-field STEM (HAADF-STEM) image in Fig. 1(c) depicts the SSO film on the STO substrate. Atomic resolution HAADF-STEM images further suggest that the SSO film is single crystalline with Ruddlesden–Popper (RP) defects running throughout the film thickness (with slightly dense and sparse regions averaging about 40-nm apart).[22,23] These RP defects are primarily oriented along [001]; thus, their impacts on the through-plane thermal transport are presumably negligible. XRD rocking curve measurements were also conducted for the STO substrate, as detailed in Sec. 3 of the supplementary material.

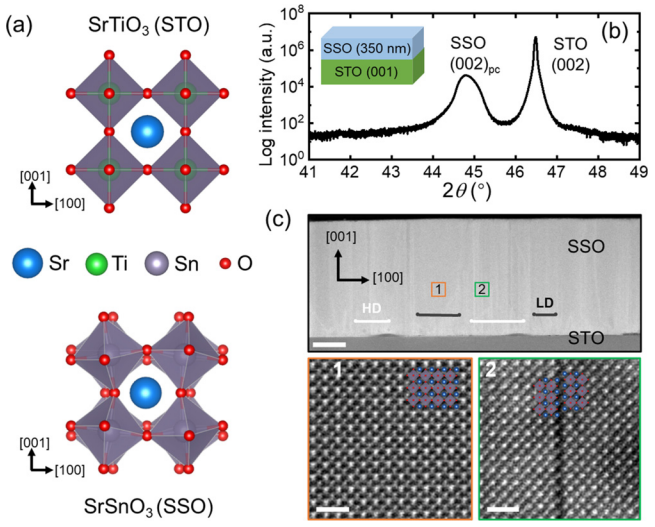

FIG. 1. (a) Lattice structures of cubic $SrTiO_3$ and orthorhombic $SrSnO_3$ with octahedral titling. (b) Room-temperature HRXRD 2θ-ω coupled scans of $SrSnO_3$/$SrTiO_3$(001), suggesting the phase-pure and single crystalline SSO film. The inset in (b) depicts the schematic of the sample stack. (c) HAADF-STEM cross-sectional images of the SSO film (350 nm) on top of the STO substrate. The scale bar is 100 nm. The line features in the low-magnification image are Ruddlesden–Popper defects. A few high-density (HD) and low-density (LD) defects regions are marked. Atomic resolution images below show the expected crystalline structure of the SSO film (region 1) and a Ruddlesden–Popper defect (region 2). Scale bars are 1 nm.

We used TDTR to measure the through-plane thermal conductivity (Λ_{SSO}, along [001]) of the single crystalline SSO film from 90 to 500 K. Over this temperature range, SSO remains orthorhombic without any phase transition. More details of the TDTR metrology are provided elsewhere.[17,24–31] Prior to TDTR measurements, an aluminum (Al) layer was sputtered onto the sample as a transducer. A reference of 300-nm SiO_2/Si and a bulk STO substrate were placed next to the sample for transducer preparation, as control samples for thermal measurements. For TDTR measurements, a 5× objective lens with a $1/e^2$ radius of ≈12 μm was used to focus both pump and probe beams onto the sample surface. The pump excitation was modulated at two frequencies ($f = 9$ and 18 MHz). Thermal transport in the sample stack is considered as thermal wave propagation at the modulation frequency producing a thermal penetration depth of $\delta = \sqrt{\Lambda/\pi f C}$, with Λ and C being the thermal conductivity and volumetric heat capacity of the sample, respectively. At ~150 K and above, δ is less than the film thickness ($d_{SSO} = 350$ nm); thus, the SSO film is *thermally opaque* [Fig. 2(a), left panel]. In this case, TDTR measurements are sensitive to Λ_{SSO} and the interfacial thermal conductance of Al/SSO (G_1). As the temperature decreases, δ may become larger than d_{SSO} due to the increased Λ_{SSO} and decreased C_{SSO} at low temperatures. Therefore, the SSO film is "*thermally thin*" and TDTR measurements also probe the thermal interface of SSO/STO (G_2) and Λ_{STO} [Fig. 2(a), right panel]. In this case, the dual-frequency TDTR analysis is used to ensure the accuracy and reliability of the data reduction at low temperatures.[32,33]

For TDTR measurements, the samples were mounted on a temperature-control stage in an environmental chamber. Measurements were first conducted on the STO substrate to obtain its temperature-dependent (T-dependent) Λ_{STO}, followed by the measurements of the SSO/STO stack. The setting temperature (T_{set}) varied from 90 to 500 K with the lowest temperature being limited by liquid nitrogen as the coolant. The actual temperature of the sample consists of three parts: T_{set}, the steady-state temperature rise (ΔT_{ss}),[24] and per-pulse temperature rise (ΔT_{pp}). At low temperatures, ΔT_{pp} can substantially impact the sample temperature due to the reduced heat capacity. Therefore, the nominal T_{set} is corrected to reflect the actual temperature of the sample accordingly in the data analysis (Sec. 4 of the supplementary material).

For data reduction, several input parameters are needed for extracting Λ_{SSO}.[17,24–31] The RT electrical conductivity of the Al transducer is obtained from the 4-point probe measurements of the SiO_2/Si reference and then converted to the RT Λ_{Al} using the Wiedemann–Franz law. The T-dependent Λ_{Al} is derived based on the linear temperature dependence of the Al electrical resistivity. The T-dependent Λ_{STO} is obtained from TDTR measurements of the STO substrate. The thickness of Al ($d_{Al} = 74$ nm) is determined from picosecond acoustics [Fig. 2(b)],[17,25–31,34] and the thickness of the SSO film ($d_{SSO} = 350$ nm) is obtained from STEM. The T-dependent C_{Al} and C_{STO} are taken from literature,[35,36] and C_{SSO} is calculated based on the Debye model (Sec. 5 of the supplementary material).[37]

Figure 2(c) depicts the representative TDTR ratio ($-V_{in}/V_{out}$) signals of the SSO film measured at RT. The black and red solid lines are the best fits for the measurement data, calculated based on a 3D thermal diffusion model.[17,24–31] The resulting RT through-plane Λ_{SSO} is 4.4 ± 0.4 W m^{-1} K^{-1}, comparable with the value previously

13 May 2024 18:59:04

Published under an exclusive license by AIP Publishing

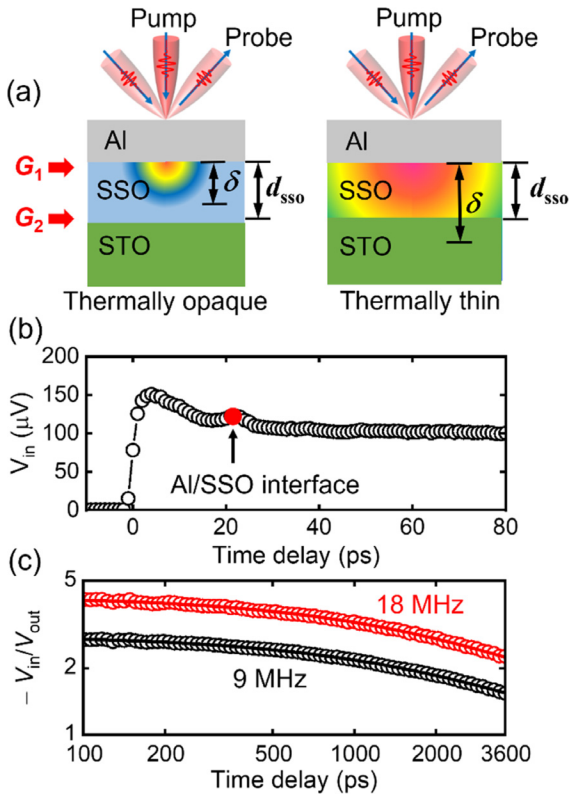

FIG. 2. (a) The 2D schematics illustrating the comparison between the SSO film thickness (d_{sso}) and thermal penetration depth (δ) for the sample stack under the thermally opaque (left) and thermally thin (right) regimes. (b) Representative TDTR in-phase signal at early time delay illustrating picosecond acoustics measurements. The red dot denotes the time delay when the longitudinal acoustic echo reflected at the Al/SSO interface arrives at the Al surface. (c) Representative TDTR ratio signals at RT with simultaneous two-frequency fitting.

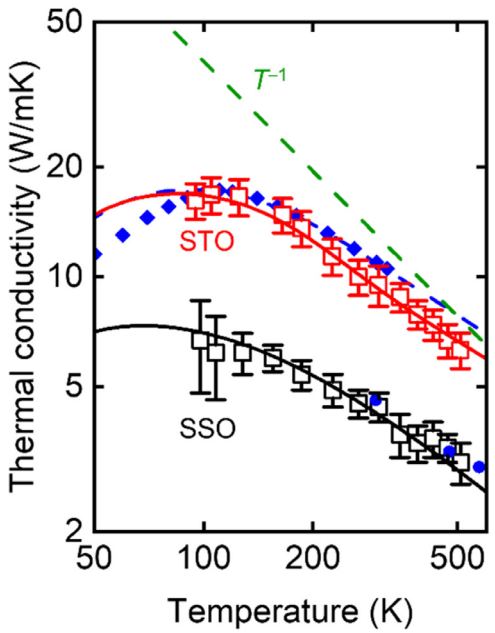

FIG. 3. Temperature-dependent thermal conductivities of the 350-nm SSO film (black squares) and the STO substrate (red squares). For comparison, literature data of Λ_{SSO} (blue circles) for micro-sized polycrystalline SSO and Λ_{STO} for bulk single crystalline STO (blue diamonds) are also presented.[14,18] The solid curves are the fits based on the Debye–Callaway model. The green dashed line follows the T^{-1} trend as a guide to the eye.

reported for polycrystalline SSO (4.5 W m^{-1} K^{-1}) with grain sizes of several micrometers.[18] This suggests the RT Λ_{SSO} of our 350-nm single crystalline SSO film approaches the bulk limit, considering that the dominant phonon mean free paths are on the order of several tens of nanometers in most perovskite oxides.[38] In addition, we notice that the RT Λ_{SSO} is significantly lower than the bulk thermal conductivities of several other perovskite oxides with the typical ABO_3 structure such as STO (11 W m^{-1} K^{-1}),[14] LAO (13 W m^{-1} K^{-1}),[16,17] and BSO (~13 W m^{-1} K^{-1}).[12,13]

To reveal the origins of the much lower Λ_{SSO} as compared with that of STO, we conducted T-dependent thermal measurements of both the SSO film and the STO substrate from 90 to 500 K. The results are plotted in Fig. 3, together with literature data of the thermal conductivities for polycrystalline SSO and bulk single crystalline STO.[14,16,18] At intermediate and high temperatures (≥150 K), the SSO film is thermally opaque, and the overall uncertainty of Λ_{SSO} from TDTR is ~10%. For temperatures <150 K, the SSO film becomes thermally thin. Correspondingly, the measurement sensitivities to G_2 and C_{SSO} increase, leading to larger errors propagated into the overall uncertainty of Λ_{SSO} (~30%). For the bulk STO substrate, the uncertainty of Λ_{STO} remains ~10% for the entire temperature range. More details of the uncertainty analysis are provided in Sec. 6 of the supplementary material.

From Fig. 3, the TDTR derived Λ_{STO} (red squares) exhibits a similar trend as compared with literature data (blue diamonds) with a peak temperature present at ~100 K. The measured T-dependent Λ_{STO} is a bit lower at intermediate and high temperatures compared with literature data.[14] We attribute the lower Λ_{STO} of our own STO substrate to the enhanced phonon-point defect scattering for this temperature range (Sec. 7 of the supplementary material). The T-dependent Λ_{STO} is then used as input parameters for extracting Λ_{SSO} from 90 to 500 K (black squares). Compared with the literature Λ_{SSO} of micro-sized polycrystalline SSO (black circles) from RT to 500 K, our measurement results suggest the bulk-like behavior of the 350-nm SSO film at RT and above.[18] After the peak temperature, both Λ_{STO} and Λ_{SSO} decrease with temperature following ~$T^{-0.74}$ and ~$T^{-0.54}$, respectively, deviating from the typical T^{-1} trend of thermal conductivity for materials with phonons as the dominant heat carriers.[33,39] It was reported previously that the deviation from T^{-1} can be partially attributed to the higher-order phonon scattering and anharmonic phonon normalization in strongly anharmonic materials.[40,41] More discussions are provided in Sec. 8 of the supplementary material on the T-dependent exponents of Λ_{STO} and Λ_{SSO}.

To gain some physical insight into the T-dependent Λ_{SSO}, we use the Debye–Callaway (D–C) model assuming a truncated linear dispersion to interpret our measurement data (Sec. 7 of the supplementary material).[42–44] In this model, the scattering rates due to normal scattering, boundary scattering, Umklapp scattering, and phonon-point

13 May 2024 18:59:04

Published under an exclusive license by AIP Publishing

defect scattering are considered. The three types of resistive scattering rates are determined by the characteristic dimension (L_c) of the sample, the Gruneisen parameters (γ_i), and the mass-fluctuation phonon-scattering parameter (Γ), respectively.

The best fits to the measured T-dependent Λ_{STO} and Λ_{SSO} from the D–C model are plotted as solid curves in Fig. 3. For STO, the truncated Debye frequencies (ω_D), sound velocities (v), and γ are taken from the literature.[45–47] The fitting parameters are L_c and point-defect concentrations. For the 350-nm SSO film, L_c is taken as the film thickness. The truncated ω_D and v are also taken from the literature.[37,48] In this case, γ and point-defect concentrations (related to Γ) are the tunable parameters to be derived from fitting. The detailed information about the parameters used in the D–C model analyses is summarized in Table I. For STO and SSO, both Sr and oxygen vacancies are possible forms of point defects. Sr-by-Sn substitutions are considered impossible owing to the large difference between the ionic radii of Sr^{2+} and Sn^{2+}. Therefore, our model analyses explore the possible combinations of Sr and oxygen vacancies as point defects.[49,50]

As shown in Fig. 3, the D–C model analyses for STO and SSO agree well with TDTR measurement results. The peak temperature of STO (~90–100 K) is reflected in TDTR measurements and well captured by the model. While the peak temperature of SSO is not apparent in measurements due to the limited temperature range, yet the model yields a temperature peak occurring at ~70 K. For the characteristic dimension, the best fit gives $L_c = 884$ nm for STO, suggesting the possible existence of domain boundaries within the bulk STO, which could lead to enhanced phonon-boundary scattering (Sec. 3 of the supplementary material). For phonon-point defect scattering, the best fit based on the D–C model analyses gives a combination of ~3% Sr vacancies and ~1% oxygen vacancies for STO, and a combination of ~2% Sr vacancies and ~0.5% oxygen vacancies for SSO. The relation between the concentration of Sr and oxygen vacancies is given by charge neutrality.[51] The mass-fluctuation phonon-scattering parameters are $\Gamma = 0.0416$ for STO and $\Gamma = 0.0127$ for SSO. In addition to vacancies, other additive atoms, such as Ca, Fe, or Al, are likely to present in bulk single crystalline STO, which can also act as point defects to suppress thermal transport.[52,53] The phonon-point defect scattering due to such possible additive atoms is not considered in the D–C model analyses. This is partially responsible for the higher point defect concentrations of Sr and O vacancies for STO derived from the D–C model analyses, as compared with literature reported vacancy concentrations for bulk single crystalline STO. Here, we acknowledge that the D–C model is empirical, not as accurate as first-principles calculations. Therefore, we implement the D–C model analyses for qualitative interpretation of the thermal measurement results to identify the dominant factors responsible for the suppressed thermal transport in SSO. Obviously, the difference in the point-defect concentrations for SSO and STO is not the main reason for the much smaller Λ_{SSO}.

For the Gruneisen parameters, the fitting for SSO yields $\gamma_L = 2.85$ and $\gamma_T = 0.86$ as nominal values, both of which are larger than the reported values for STO: $\gamma_L = 2.6$ and $\gamma_T = 0.7$.[45] Based on Eq. (S7), a larger Gruneisen parameter leads to a higher phonon scattering rate. This is reasonable considering that the phonon scattering is a result of anharmonicity, which is tied to the lattice symmetry. Several ABO_3 perovskite oxides, including STO and BSO, have the cubic perovskite structure with the space group of $Pm\bar{3}m$.[54,55] While for SSO, the tilted SnO_6 octahedra lead to a distorted orthorhombic lattice structure ($Pnma$) with a lowered symmetry and, thus, enhance the anharmonicity for phonon–phonon Umklapp scattering [Fig. 1(a)].[19,56] In addition, based on a model sensitivity analysis using the parameters listed in Table I, we identify the lower Debye temperatures of SSO as the dominant factor responsible for the smaller RT Λ_{SSO} along [001] compared to Λ_{STO}. These lower Debye temperatures correspond to lower phonon cutoff frequencies at the Brillouin zone boundary, as reflected in the phonon dispersions of STO and SSO,[46,48] which are again directly impacted by the lattice symmetry. More detailed discussions of the Gruneisen parameters and model sensitivity analysis for the determination of dominant factors are provided in Sec. 7 of the supplementary material.

In addition to thermal conductivity, we can also extract the interfacial thermal conductance from TDTR. G_1 for the Al/SSO interface changes from 75 to 100 MW m^{-2} K^{-1} as the temperature increases from 90 to 500 K. Our measured G_1 values are lower than those predicted from the DMM, and the discrepancy becomes larger at elevated temperatures (Sec. 8 of the supplementary material). This discrepancy is likely attributed to the insufficient SSO surface treatment prior to the Al deposition, which can presumably lead to a lower G_1 when compared with the DMM model.

In summary, we systematically investigated the thermal transport properties of single crystalline SSO and established the structure-thermal property relationship. The pristine 350-nm SSO film has a thermal conductivity of 4.4 ± 0.4 W m^{-1} K^{-1} along [001] at room temperature, approaching the bulk limit. By integrating T-dependent thermal measurement and detailed Debye–Callaway model analyses, we reveal the fundamental mechanisms responsible for the lower thermal conductivity of single crystalline SSO, compared with that of STO. The distorted orthorhombic structure of SSO with the tilted SnO_6 octahedra reduces the lattice symmetry and modifies the phonon dispersion. The resulting phonon frequencies at the Brillouin zone boundary are significantly reduced, which correspondingly lead to the lower Debye temperatures for SSO. The thermal study in this work provides insight into the thermal transport mechanisms in perovskite oxides and enhances the thermal design of SSO-based electronic devices.

TABLE I. Parameters in the Debye–Callaway model. The subscripts of L and T denote the values for the longitudinal and acoustic phonon branches, respectively.

	$\theta_{D,L}$ (K)	$\theta_{D,T}$ (K)	$\omega_{D,L}$ (THz)	$\omega_{D,T}$ (THz)	v_L (m/s)	v_T (m/s)	γ_L	γ_T	L_c (nm)	Γ (10^{-4})	RT Λ (W m^{-1} K^{-1})
STO[11]	192[46]	173[46]	25.1	22.6	8500	5200	2.6[45]	0.7[45]	590	227	10.9[14]
STO	192[46]	173[46]	25.1	22.6	8500	5200	2.6[45]	0.7[45]	884	416	9.3
SSO	141[48]	108[48]	18.2	14.1	7216	4170	2.85	0.86	350	127	4.2

13 May 2024 18:59:04

Published under an exclusive license by AIP Publishing

See the supplementary material for details of the sample synthesis, structural characterization, thermal measurements and data reduction, measurement sensitivity and uncertainty analysis, comparison with literature data, and the D–C modeling calculations.

The authors gratefully acknowledge the funding support from the National Science Foundation through the MRSEC Program (Award No. DMR-2011401). X.X. appreciates the partial support from NSF (Award No. CBET-2226579). Parts of this work were carried out at the UMN Characterization Facility, supported in part by the NSF through the UMN MRSEC Program. Part of the work was supported by the Air Force Office of Scientific Research (AFOSR) through Grant Nos. FA9550-21-1-0025, and FA9550-23-1-0247. Portions of this work were conducted in the Minnesota Nano Center, supported by the NSF through the National Nanotechnology Coordinated Infrastructure (NNCI) under Award No. ECCS-2025124. The authors appreciate valuable discussions with Professor Tianli Feng and Professor Zhibin Gao, and Ms. Xiaoying Wang, on the four-phonon scattering.

AUTHOR DECLARATIONS

Conflict of Interest

The authors have no conflicts to disclose.

Author Contributions

Chi Zhang: Data curation (lead); Formal analysis (lead); Methodology (lead); Writing – original draft (lead); Writing – review & editing (lead). **Fengdeng Liu:** Data curation (supporting); Formal analysis (supporting); Methodology (supporting); Writing – original draft (supporting); Writing – review & editing (supporting). **Silu Guo:** Data curation (supporting); Formal analysis (supporting); Methodology (supporting); Writing – original draft (supporting); Writing – review & editing (supporting). **Yingying Zhang:** Formal analysis (supporting); Methodology (supporting); Writing – review & editing (supporting). **Xiaotian Xu:** Formal analysis (supporting); Writing – review & editing (supporting). **K. Andre Mkhoyan:** Funding acquisition (equal); Project administration (supporting); Supervision (equal); Writing – original draft (supporting); Writing – review & editing (supporting). **Bharat Jalan:** Conceptualization (equal); Funding acquisition (equal); Project administration (supporting); Supervision (equal); Writing – original draft (supporting); Writing – review & editing (supporting). **Xiaojia Wang:** Conceptualization (equal); Funding acquisition (equal); Project administration (lead); Supervision (equal); Writing – original draft (supporting); Writing – review & editing (supporting).

DATA AVAILABILITY

The data that support the findings of this study are available within the article or from the corresponding author upon reasonable request.

REFERENCES

[1]H. J. Kim, U. Kim, T. H. Kim, J. Kim, H. M. Kim, B.-G. Jeon, W.-J. Lee, H. S. Mun, K. T. Hong, and J. Yu, Phys. Rev. B **86**(16), 165205 (2012).
[2]H. Paik, Z. Chen, E. Lochocki, A. Seidner, A. Verma, N. Tanen, J. Park, M. Uchida, S. Shang, and B.-C. Zhou, APL Mater. **5**(11), 116107 (2017).
[3]A. Prakash, P. Xu, A. Faghaninia, S. Shukla, J. W. Ager, C. S. Lo, and B. Jalan, Nat. Commun. **8**(1), 15167 (2017).
[4]W.-J. Lee, H. J. Kim, J. Kang, D. H. Jang, T. H. Kim, J. H. Lee, and K. H. Kim, Annu. Rev. Mater. Res. **47**, 391 (2017).
[5]T. Truttmann, A. Prakash, J. Yue, T. E. Mates, and B. Jalan, Appl. Phys. Lett. **115**(15), 152103 (2019).
[6]T. Wang, A. Prakash, Y. Dong, T. Truttmann, A. Bucsek, R. James, D. D. Fong, J.-W. Kim, P. J. Ryan, and H. Zhou, ACS Appl. Mater. Interfaces **10**(50), 43802 (2018).
[7]H. Mizoguchi, H. W. Eng, and P. M. Woodward, Inorg. Chem. **43**(5), 1667 (2004).
[8]A. Prakash, N. F. Quackenbush, H. Yun, J. Held, T. Wang, T. Truttmann, J. M. Ablett, C. Weiland, T.-L. Lee, and J. C. Woicik, Nano Lett. **19**(12), 8920 (2019).
[9]W. Zhang, J. Tang, and J. Ye, J. Mater. Res. **22**(7), 1859 (2007).
[10]T. K. Truttmann, J.-J. Zhou, I.-T. Lu, A. K. Rajapitamahuni, F. Liu, T. E. Mates, M. Bernardi, and B. Jalan, Commun. Phys. **4**(1), 241 (2021).
[11]V. S. K. Chaganti, A. Prakash, J. Yue, B. Jalan, and S. J. Koester, IEEE Electron Device Lett. **39**(9), 1381 (2018).
[12]L. Chen, Y. Zhang, X. Wang, B. Jalan, S. Chen, and Y. Hou, J. Phys. Chem. C **122**(21), 11482 (2018).
[13]A. Prakash, P. Xu, X. Wu, G. Haugstad, X. Wang, and B. Jalan, J. Mater. Chem. C. **5**(23), 5730 (2017).
[14]C. Yu, M. L. Scullin, M. Huijben, R. Ramesh, and A. Majumdar, Appl. Phys. Lett. **92**(19), 191911 (2008).
[15]D.-W. Oh, J. Ravichandran, C.-W. Liang, W. Siemons, B. Jalan, C. M. Brooks, M. Huijben, D. G. Schlom, S. Stemmer, and L. W. Martin, Appl. Phys. Lett. **98**(22), 221904 (2011).
[16]E. Langenberg, E. Ferreiro-Vila, V. Leborán, A. Fumega, V. Pardo, and F. Rivadulla, APL Mater. **4**(10), 104815 (2016).
[17]X. Wu, J. Walter, T. Feng, J. Zhu, H. Zheng, J. F. Mitchell, N. Biškup, M. Varela, X. Ruan, and C. Leighton, Adv. Funct. Mater. **27**(47), 1704233 (2017).
[18]M. Yasukawa, K. Ueda, S. Fujitsu, and H. Hosono, Ceram. Int. **43**(13), 9653 (2017).
[19]T. Wang, L. R. Thoutam, A. Prakash, W. Nunn, G. Haugstad, and B. Jalan, Phys. Rev. Mater. **1**(6), 061601 (2017).
[20]E. H. Mountstevens, J. P. Attfield, and S. A. Redfern, J. Phys. Condens. Matter. **15**(49), 8315 (2003).
[21]T. K. Truttmann, F. Liu, J. Garcia-Barriocanal, R. D. James, and B. Jalan, ACS Appl. Electron. Mater. **3**(3), 1127 (2021).
[22]S. Ruddlesden and P. Popper, Acta Cryst. **10**(8), 538 (1957).
[23]S. Ruddlesden and P. Popper, Acta Cryst. **11**(1), 54 (1958).
[24]D. G. Cahill, Rev. Sci. Instrum. **75**(12), 5119 (2004).
[25]J. Zhu, H. Park, J. Y. Chen, X. Gu, H. Zhang, S. Karthikeyan, N. Wendel, S. A. Campbell, M. Dawber, and X. Du, Adv. Electron. Mater. **2**(5), 1600040 (2016).
[26]Y. Zhang, Q. Su, J. Zhu, S. Koirala, S. J. Koester, and X. Wang, Appl. Phys. Lett. **116**(20), 202101 (2020).
[27]Y. Zhang, M. A. Eslamisaray, T. Feng, U. Kortshagen, and X. Wang, Nanoscale Adv. **4**(1), 87 (2022).
[28]J. Zhu, Y. Zhu, X. Wu, H. Song, Y. Zhang, and X. Wang, Appl. Phys. Lett. **108**(23), 231903 (2016).
[29]X. Wu, B. L. Greenberg, Y. Zhang, J. T. Held, D. Huang, J. G. Barriocanal, K. A. Mkhoyan, E. S. Aydil, U. Kortshagen, and X. Wang, Phys. Rev. Mater. **4**(8), 086001 (2020).
[30]J. Zhu, T. Feng, S. Mills, P. Wang, X. Wu, L. Zhang, S. T. Pantelides, X. Du, and X. Wang, ACS Appl. Mater. Interfaces **10**(47), 40740 (2018).
[31]T. Feng, X. Wu, X. Yang, P. Wang, L. Zhang, X. Du, X. Wang, and S. T. Pantelides, Adv. Funct. Mater. **30**(5), 1907286 (2020).
[32]P. Jiang, B. Huang, and Y. K. Koh, Rev. Sci. Instrum. **87**(7), 075101 (2016).
[33]Y. Zhang, W. M. Postiglione, R. Xie, C. Zhang, H. Zhou, V. Chaturvedi, K. Heltemes, H. Zhou, T. Feng, and C. Leighton, Nat. Commun. **14**(1), 2626 (2023).
[34]G. T. Hohensee, W.-P. Hsieh, M. D. Losego, and D. G. Cahill, Rev. Sci. Instrum. **83**(11), 114902 (2012).
[35]D. Ditmars, C. Plint, and R. Shukla, Int. J. Thermophys. **6**(5), 499 (1985).

13 May 2024 18:59:04

Published under an exclusive license by AIP Publishing

[36]Y. Touloukian and E. Buyco, *Thermophysical Properties of Matter-The TPRC Data Series. Volume 5. Specific Heat-Nonmetallic Solids* (Thermophysical and Electronic Properties Information Analysis Center, Lafayette, IN, 1970).
[37]D. Cherrad, M. Maouche, M. Maamache, and L. Krache, Phys. B: Condens. Matter **406**(14), 2714 (2011).
[38]A. Negi, A. Rodriguez, X. Zhang, A. H. Comstock, C. Yang, D. Sun, X. Jiang, D. Kumah, M. Hu, and J. Liu, Adv. Sci. **10**, 2301273 (2023).
[39]X. Wang, V. Ho, R. A. Segalman, and D. G. Cahill, Macromolecules **46**(12), 4937 (2013).
[40]J. Tiwari and T. Feng, Phys. Rev. Mater. **7**(6), 065001 (2023).
[41]X. Wang, Z. Gao, G. Zhu, J. Ren, L. Hu, J. Sun, X. Ding, Y. Xia, and B. Li, Phys. Rev. B **107**(21), 214308 (2023).
[42]G. A. Slack, Phys. Rev. **126**(2), 427 (1962).
[43]D. Morelli, J. Heremans, and G. Slack, Phys. Rev. B **66**(19), 195304 (2002).
[44]P. Jiang, X. Qian, X. Li, and R. Yang, Appl. Phys. Lett. **113**(23), 232105 (2018).
[45]A. Beattie and G. Samara, J. Appl. Phys. **42**(6), 2376 (1971).
[46]W. Stirling, J. Phys. C: Solid State Phys. **5**(19), 2711 (1972).
[47]R. Wilson, B. A. Apgar, W.-P. Hsieh, L. W. Martin, and D. G. Cahill, Phys. Rev. B **91**(11), 115414 (2015).
[48]M. A. Sattar, M. Benkraouda, and N. Amrane, Phys. B: Condens. Matter **590**, 412216 (2020).
[49]T. Wang, K. C. Pitike, Y. Yuan, S. M. Nakhmanson, V. Gopalan, and B. Jalan, APL Mater. **4**(12), 126111 (2016).
[50]S. Suzuki, A. Honda, N. Iwaji, S. I. Higai, A. Ando, H. Takagi, H. Kasatani, and K. Deguchi, Phys. Rev. B **86**(6), 060102 (2012).
[51]A. Faghaninia, J. W. Ager III, and C. S. Lo, Phys. Rev. B **91**(23), 235123 (2015).
[52]N. H. Chan, R. Sharma, and D. M. Smyth, J. Electrochem. Soc. **128**(8), 1762 (1981).
[53]P. Ambwani, P. Xu, G. Haugstad, J. Jeong, R. Deng, K. Mkhoyan, B. Jalan, and C. Leighton, J. Appl. Phys. **120**(5), 055704 (2016).
[54]A. Bhalla, R. Guo, and R. Roy, Mater. Res. Innov. **4**(1), 3 (2000).
[55]H. Mizoguchi, P. M. Woodward, C.-H. Park, and D. A. Keszler, J. Am. Chem. Soc. **126**(31), 9796 (2004).
[56]B. Veličkov, V. Kahlenberg, R. Bertram, and M. Bernhagen, Z. Kristallogr. **222**(9), 466 (2007).

13 May 2024 18:59:04

Published under an exclusive license by AIP Publishing